



Development of cutting edge geometries for hard milling operations



B. Denkena, J. Köhler, B. Bergmann*

Institute of Production Engineering and Machine Tools (IFW), Leibniz Universität Hannover, An der Universität 2, 30823 Garbsen, Germany

ARTICLE INFO

Article history:

Available online 23 November 2014

Keywords:

Milling
Failure
Finite element method (FEM)
Tool geometry
Residual stress

ABSTRACT

Milling of hardened steels is a challenging task for mould and die manufacturing due to the high material strength. One major drawback is the tool wear, which is a result of the high thermo-mechanical stress on the tool. The wear rate can generally be influenced by the tool geometry, coatings and substrates. A further approach is to modify the flank face of the tool, which leads to geometrical limitation of the flank wear. The challenge of this approach is to design flank face modifications, which offer process reliability and increased performance. Against this backdrop a finite element simulation has been constructed to analyze tool stresses. Therefore, different material and friction models were investigated. Based on this simulation a regression model has been developed. Due to the regression model the flank face modifications have been designed and manufactured by laser machining. In cutting tests the potential of the flank face modifications compared to conventional hard milling tools was investigated. The flank face modifications enable the increase of tool life time and the production of workpieces with reduced tensile residual stresses.

© 2014 CIRP.

Introduction

In production industry, especially in die and mould engineering, steel parts are used, which are subjected to high loads and therefore are hardened or quenched and tempered [1].

After heat treatment the final contour has to be manufactured. Apart from abrasive processes, machining with geometrically defined cutting edges is established to machine hardened steel components as a substitution method. The advantages of hard machining compared to grinding are high removal rates, short machining times, a flexible process design and eschewal of coolant. However, a disadvantage of hard machining is an increased tool wear compared to machining materials in none hardened state. Under these conditions hard milling presents a particular challenge due to the dynamical thermo-mechanical load at the cutting edge. Current research aims to increase the tool life in hard machining. Besides the choice of the tool substrate and the machining parameters, the geometric design of the cutting edge significantly influences the wear behaviour [2,3].

A variety of researchers have shown that the use of a negative rake angle increases the tool life due to induced compressive loads on the tool cutting edge [4–6]. Besides the investigations regarding tool wear, surface quality in hard machining has been in focus

[7]. Due to the fact, that hardened components are exposed to high loads, the surface quality and surface integrity have to present required characteristics. Thereby, the tool wear has a significant influence on the surface integrity of the component. Increasing flank wear leads to increased thermo-mechanical stress and thus to an increase of tensile residual stresses on the workpiece surface [8]. An approach to influence both disadvantages, residual stresses and tool life, has been achieved by specific modification of the tool flank face as shown in Fig. 1. Here, an undercut of the flank face limits the wear on the defined area of the cutting edge. Consequently, by a systematic tool development, a rise in efficiency can be achieved in hard turning [8,9]. However, due to the flank face modification the mechanical stability of the cutting edge is reduced. For designing these tools, the knowledge of the stresses in the undercut is necessary. In experiments these stress values can be only detected with higher complexity. Hence finite element simulations are a suitable tool to avoid tool fracture at the undercut and to analyze the influence of specific cutting edge geometries in machining.

In addition, due to simulations, cost and time intensive experimental investigations can be reduced [3,10,11].

Many studies deal with the calculation of thermo-mechanical loads of the cutting tools using solid-state simulations, which are based on the finite elements method [3,11]. Denkena [12] and Scherbarth [13] interpreted the tool wear and additional tool failure based on the principal stress hypothesis, which were analyzed by using solid-state simulations. Thus, tool failure

* Corresponding author. Tel.: +49 51176218066.

E-mail address: bergmann@ifw.uni-hannover.de (B. Bergmann).

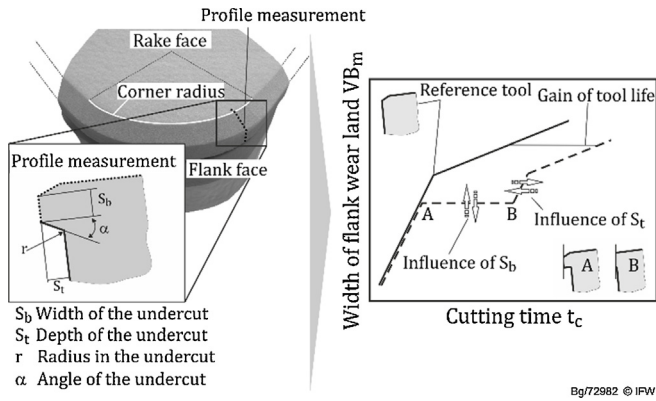


Fig. 1. Definition of flank face modification and effect on tool wear.

appears if the first principal stress exceeds the tensile strength of the tool substrate. This was also demonstrated by Zhou et al. [14]. Accordingly, optimized chamfer geometry leads to reduced minimal principle stresses in the wedge, which favours tool life time. This was also shown in hard turning AISI H13. Thus higher tool life time occurs due to reduced tensile principle stresses by applying chamfered cutting edges [15]. Further application of chip formation simulations according to the design of the cutting edge, especially rounded cutting edges, can be found in [16–18]. Thus the reduced stresses in the wedge lead to higher tool lifetime.

By using the chip formation simulation Meyer designed the flank face modification for hard turning operations [8]. However, a comparison of the calculated stresses with tool failure was not executed. This paper deals with the modelling of a hard milling operation by means of chip formation simulation for tools with a flank face modification. Besides the approximation of the milling operation to a two-dimensional orthogonal turning process, the tool failure is interpreted by the calculated tool stresses. Afterwards the designed tool was investigated regarding its wear behaviour in hard milling AISI H13.

Experimental setup

Experimental cutting tests were carried out on a Heller 4-Axes Machining Centre MC16 in face milling operations without coolant. As workpiece material AISI H13 hot work steel was used. The material possesses a martensitic microstructure with finely dispersed carbides. With a value of 56 HRC maximum attainable hardness of hot-work steel was used. The properties of hardened AISI H13 are listed in Table 1.

Due to the high strength, good resistance to thermo softening, heat checking, high hardenability and high toughness, AISI H13 is widely used as material for dies [19]. The experiments have been conducted with a single tooth face mill. Inserts with round geometry of the type RPHW1204M0T with a PVD TiAlN-coating were used. The properties of the cutting tool, based on data from the manufacturer and literature, are summarized in Table 2. The reference tool geometry and the modified geometries were characterized by SEM and tactile measurement. The reference tools were provided by an angle of chamfer $\gamma_f = -20^\circ$ and a chamfer

Table 1
Mechanical properties of hardened AISI H13.

Tensile strength R_m [N/mm ²]	Yield strength $R_{p0.2\%}$ [N/mm ²]	Young's modulus E [GPa]	Hardness [HRC]
2006	1515	211	56

Table 2

Thermal and mechanical properties of the workpiece and tool.

Parameters	Workpiece (AISI H13)	Cutting tool (WC)
Young's modulus (GPa)	211	678***
Poisson's ratio	0.28*	0.22***
Density (kg/m ³)	7800*	14,800***
Specific heat (J/kg K)	$420 + 0.504T$ (T in $^\circ\text{C}$)	196**
Thermo conductivity (W/mK)	28.4 (350 $^\circ\text{C}$); 28.4 (475 $^\circ\text{C}$); 28.7 (605 $^\circ\text{C}$)	129***
Hardness (HRC/HV30)	56 HRC	1782 HV30***
Thermo expansion ($10^{-6}/^\circ\text{C}$)		4.63***
Compressive strength		~ 6500 MPa**
Fracture toughness (MPa $\sqrt{\text{m}}$)		9.44***

* Data from [25].

** Data from [26].

*** Data from tool manufacturer SECO tools.

width of $b_n = 0.20$ mm, cutting edge radius exhibits a value of $r_\beta = 30$ μm . The modification of the flank face, the so called undercut, was performed with laser machining on a Sauer Lasertec 40 Precision Tool. In preliminary studies it was ensured that the method of preparation of the laser did not affect the substrate properties and wear behaviour of the cutting tools. The accuracy of the laser machined undercut geometries was about 5 μm , which only depends on the optical set up for reference point. However, rectangular undercuts and without a rounding could not produced due to the properties of the laser source and the hardness of the cemented carbide.

The face mill diameter is $D = 25$ mm. Because of round cutting inserts the diameter depends on the depth of cut. In this investigation constant depth of cut $a_p = 0.5$ mm was used, which results in an effective diameter of $D_{\text{eff}} = 17.8$ mm. As reference process parameter a cutting speed of $v_c = 120$ m/min, feed per tooth $f_z = 0.2$ mm and width of cut $a_e = 5$ mm was applied, which is comparable to hard milling parameters in industry.

For wear detection a digital microscope Keyence VHX-600 and a scanning electron microscope Zeiss EVO 60 VP (SEM) were used. Tool life criteria has been defined as a maximum flank wear land width of $VB_m = 200$ μm or the occurrence of tool failure. Process forces were measured by a 3-component-dynamometer of type Kistler 9257B. Residual stresses of the workpiece were determined by X-ray diffractometer analysis, using the $\sin^2 \psi$ method.

Finite element modelling

The design of the undercut depends on the tool stresses. By using three-dimensional finite simulations tool stresses can be calculated over the cutting edge. However, three-dimensional chip formation simulations are time-consuming in comparison to two-dimensional chip formation simulations. For this reason, the milling process was approximated to an orthogonal machining process. The milling process is presented in Fig. 2. Additionally, relevant parameters are shown.

For transformation and approximation of the milling process, it is particularly important to determine the engagement parameters. Their calculation is hereinafter exhibited. As can be seen in the bottom of Fig. 2, the undeformed chip thickness varies along the cutting edge b_{eff} . The undeformed chip thickness depends on the feed motion angle φ and tool cutting edge angle κ . Thereby, the tool cutting edge angle shifts from $\kappa = 0^\circ$ up to a maximum value. Due to this the undeformed chip thickness varies from $h = 0$ over the effective undeformed chip thickness h_{eff} up to the maximum undeformed chip thickness h_1 . Here, h_{eff} differs from the average chip thickness h_m . With respect to small cutting edge angles κ Köhler [20] shows, that the cutting forces can be calculated with a higher accuracy in comparison to the approach of Kienzle due to



Fig. 2. The milling process.

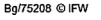


Fig. 3. Transformation of the milling process for the finite element model.

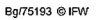


Fig. 4. Set-up for the finite element simulations.

$$h_1 = f_z \cdot \sin \varphi \cdot \sin 2\kappa_{\text{eff}} \quad (8)$$

Fig. 4 displays the chip simulation by the finite element method (FEM). The commercial software DEFORM-2D was used, which is

Overall 4000 nodes for the workpiece and 3000 nodes for the tool were used as initial mesh, consisting of quadrilateral elements. To avoid stress gradients, a finer mesh was used in the area around the deformation zone. In all simulations, fifteen nodes were set within the undeformed chip thickness. The tool was modelled as elastic. The tool was set up without coating due to the removed coating in the undercut by laser machining. This results, of course, in different stresses at the cutting edge. However, the stresses in undercut determine the wear behaviour of these tools. The workpiece was set up as plastic with a continuous remeshing. Hereby, the solution from one simulation step after remeshing was interpolated from the old mesh to the new mesh [11,23]. Continuous remeshing further avoids element distortions. When using the Lagrangian modelling method the grid deforms with the material. This is one of the main drawbacks of this method. With a large global heat transfer coefficient h the contact between tool and workpiece was modelled as thermally perfect, referring to Filice et al. [24]. The tool and workpiece properties are listed in Table 2.

In machining high strain, strain rate, strain hardening and non-linear material properties occur. To consider these effects the Johnson–Cook model was applied, which is widely used in numerical analysis, Eq. (9) [11,27].

$$\sigma = (A + B\epsilon^n) \cdot \left(1 + C \ln\left(\frac{\dot{\epsilon}}{\dot{\epsilon}_0}\right)\right) \cdot \left(1 - \left(\frac{T - T_{\text{room}}}{T_{\text{melt}} - T_{\text{room}}}\right)^m\right) \quad (9)$$

The approach links the material behaviour regarding strain, strain rate and temperature with multiplicative terms. The first term presents the strain hardening. The second term

Table 3

Material constants for the developed material model for AISI H13 tool steel by Umbrello et al. [30].

Parameter	A	B	C	D	E	N	m	T_{melt}	F	G
Value	674.8 MPa	239.2 MPa	0.027	1.16	0.88	0.28	1.3	1487 °C	232.34	94.44

Table 4

Material constants for the developed material model for AISI H13 tool steel by Yan et al. [31].

Parameter	A	B	E	N	m	T_{melt}	C	D
Value	908.54 MPa	321.39 MPa	0.028	0.278	1.18	1487 °C	21.43	537.51

demonstrates the increase in flow stress due to high strain rates. Thermal softening is represented by the third term. A , B , C , n and m are constants, which depend on the material. However, the material model by Johnson–Cook does not consider different material hardness. Especially the hardness of AISI H13 varies with its application. For instance, the hardness of dies differs to adjust the forming process and possess various material strengths. For extrusion dies 43–52 HRC, for die-casting dies 44–50 HRC and for forging dies 40–55 HRC are applied [19].

First investigations in the field of machining and simulation of AISI H13 were conducted by Ng et al. [28]. Based on Oxley's cutting theory, Shatla et al. tuned the Johnson–Cook material model [25,29], presented in Eq. (10).

$$\sigma = (A + B\varepsilon^n) \cdot \left(1 + \text{Cln}\left(\frac{\dot{\varepsilon}}{\dot{\varepsilon}_0}\right)\right) \cdot \left(D - E \cdot \left(\frac{T - T_{\text{room}}}{T_{\text{melt}} - T_{\text{room}}}\right)^m\right) \quad (10)$$

The flow stress equation is similar to the Johnson–Cook material model with additional coefficients, which are added for more flexibility of the optimization algorithm. The additional coefficients, D and E , are material constants, which are determined as well as A , B , n , C and m [25]. The material model for AISI H13 offers a good conformance between measured and simulated process forces in milling operation.

In order to use FE simulation for analysing the influence of AISI H13 in machining proper flow stress data with respect of the workpiece hardness is necessary. Therefore, Umbrello et al. [30] and Yan et al. [31] developed flow stress models with respect to the workpiece hardness. The validity of both material models could be shown in hard turning by a comparison of the simulated process forces with the experimental process forces. Albeit, a comparison of the process forces in machining AISI H13 with a material hardness of 56 HRC did not take place. For this reason, both material models have to be considered regarding their transmission for hard milling process and the material hardness of 56 HRC. Umbrello et al. enhanced a reference model, which was developed by Shatla et al., by two third order polynomial functions [30].

$$\sigma = (A + F + G\varepsilon + B\varepsilon^n) \cdot \left(1 + \text{Cln}\left(\frac{\dot{\varepsilon}}{\dot{\varepsilon}_0}\right)\right) \cdot \left(D - E \cdot \left(\frac{T - T_{\text{room}}}{T_{\text{melt}} - T_{\text{room}}}\right)^m\right) \quad (11)$$

Comparing Eq. (10) with Eq. (11) two new parameters are included, F and G , which are calculated by the empirical equations (Eqs. (12) and (13)) [30].

$$F(\text{HRC}) = -0.00283 \cdot (\text{HRC})^3 + 0.49998 \cdot (\text{HRC})^2 - 4.79458 \cdot \text{HRC} - 570.104 \quad (\text{MPa}) \quad (12)$$

$$G(\text{HRC}) = -0.0001 \cdot (\text{HRC})^3 + 0.1875 \cdot (\text{HRC})^2 - 10.6558\text{HRC} - 120.7277 \quad (\text{MPa}) \quad (13)$$

Parameter F modifies the initial yield stress and parameter G modifies the strain hardening curve. All material constants for the reference material model, including the two additional hardness based parameters F and G are summarized in Table 3. According to Shatla et al. the reference strain rate was set to $\dot{\varepsilon}_0 = 1.0 \text{ s}^{-1}$.

In comparison to Umbrello et al., Yen et al. added a function of incremental flow stress between the reference flow stress and the flow stress with those, which have a different hardness and with variation of strain [31]. They assumed an increasing yield stress and tensile strength with higher hardness, Eq. (14). Between these points logarithm behaviour was presumed. C and D , see Eqs. (15) and (16), represent the influence of hardness [31]. Depending on the experimental data by Shatla et al. the parameters were determined by regression analyses.

$$\Delta\sigma = \text{Cln}(\varepsilon_0 + \varepsilon) + D \quad (14)$$

With:

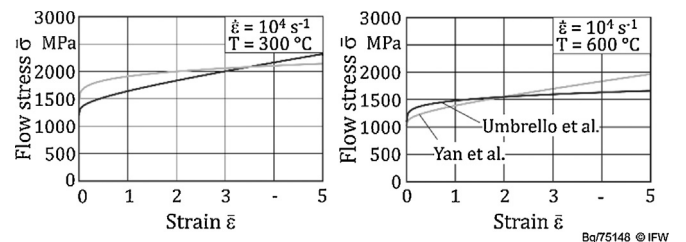
$$C(\text{HRC}) = 0.0576 \cdot (\text{HRC})^2 - 3.7861 \cdot \text{HRC} + 52.82 \quad (\text{MPa}) \quad (15)$$

$$D(\text{HRC}) = 0.6311 \cdot (\text{HRC})^2 - 12.752 \cdot \text{HRC} + 727.5 \quad (\text{MPa}) \quad (16)$$

$$\sigma = (A + B\varepsilon^n + \text{Cln}(\varepsilon_0 + \varepsilon) + D) \cdot \left(1 + \text{Eln}\left(\frac{\dot{\varepsilon}}{\dot{\varepsilon}_0}\right)\right) \cdot \left(1 - \left(\frac{T - T_{\text{room}}}{T_{\text{melt}} - T_{\text{room}}}\right)^m\right) \quad (17)$$

Table 4 summarizes the developed parameters for the material model, presented by Eq. (17). Also the reference strain rate is $\dot{\varepsilon}_0 = 1.0 \text{ s}^{-1}$. The reference strain was set to $\varepsilon_0 = 0.001$. Both material models were compared with experimental results of Ng et al. [27]. They offer a good correlation between simulated and experimental process forces. Nevertheless, there are differences between both assumptions. Fig. 5 represents the calculated flow stress as a function of strain at different temperatures and constant strain rate.

With increasing strain the flow stress increases, see Fig. 5. Further, increasing temperature occurs in thermo softening

**Fig. 5.** Flow stress for different material models.

and decreasing flow stress. Additionally, the intersection point shifts to lower strain at higher temperatures. It can be stated that both material models consider the material hardness. However, these approaches lead to different flow stresses, which have to be considered.

Friction model

Besides the material flow stress data and adjusted boundary condition, accuracy of numerical simulation depends on the assumed friction, which is often difficult to measure. The friction influences the thermo-mechanical load and has to be analyzed for an accurate simulation and was investigated in this study [18]. Different friction models have been used in literature. Nevertheless, the issue of friction in machining has not yet been solved. The Coulomb friction law describes the quotient of the tangential force F_t and normal force F_n . Alternatively, it can be expressed by the shear stress τ and normal stress σ_n (Eq. (18)) [18,32–34].

$$\mu = \frac{F_t}{F_n} = \frac{\tau}{\sigma_n} \quad (18)$$

It is assumed to be constant over the contact length between tool and workpiece. In comparison to Coulomb friction law, the shear factor model, developed by Tresca, takes the shear flow stress k into account, see Eq. (19) [34].

$$\tau = m \cdot k = \frac{m}{\sqrt{3}} \sigma_0 \quad (19)$$

Therefore, the shear factor m describes the proportional relationship between the flow stress k and the shear stress τ . Conversely to the Coulomb friction model, Tresca's friction model is independent of the pressure acting on the cutting tool. In machining simulation, the friction model can be formulated instead of the shear flow stress in terms of the flow stress of the material. Depending on the Mises flow criterion, which describes the relationship between flow stress in uniaxial tension and shear flow stress, k can be replaced by the shear yield strength of the material element at the tool-chip interface ($k_{\text{chip}} = \sigma_0/\sqrt{3}$) [18].

The shear factor m can be varied between $m = 0^\circ$ (frictionless) and $m = 1$ (sticking) [18,32–34]. Zorev introduced the terms of sticking (Eq. (20)) and sliding (Eq. (21)) according to friction into machining [35].

$$\tau(x) = k_{\text{chip}} \quad \text{if} \quad \mu \cdot \sigma_n(x) \geq m \cdot k \quad \text{for} \quad 0 < x \leq l_p \quad (20)$$

$$\tau = \mu \cdot \sigma_n(x) \quad \text{if} \quad \mu \cdot \sigma_n(x) < m \cdot k \quad \text{for} \quad l_p < x \leq l_c \quad (21)$$

Zorev defines two regions on the rake face, displayed in Fig. 6 [35].

In the sticking region shear stress is equal to yield strength of the material element at the tool-chip interface k_{chip} [18,34].

At the sliding region shear stress is proportional to the normal stress. Thereby, both regions, sticking l_p and contact length l_c depend on the tool and workpiece properties and also on machining parameters. In contrast to the sticking region the sliding region is comparably small. Besides these friction models, further models were developed [34,35].

In this study the shear factor m and the friction laws of Coulomb and Zorev are investigated. For both material models according to Umbrello et al. and Yen et al. the friction was varied for the shear factor m from 0.2 to 0.8. The same procedure was done for μ according to Coulomb's friction law. The initial parameters for Zorev's friction law were set up to $m = 0.2$ and $\mu = 0.1$. Both parameters were parallel increased in the incremental steps for $m = 0.2$ and $\mu = 0.1$. Additionally, $m = 0.5$ and $\mu = 0.3$ were analyzed.

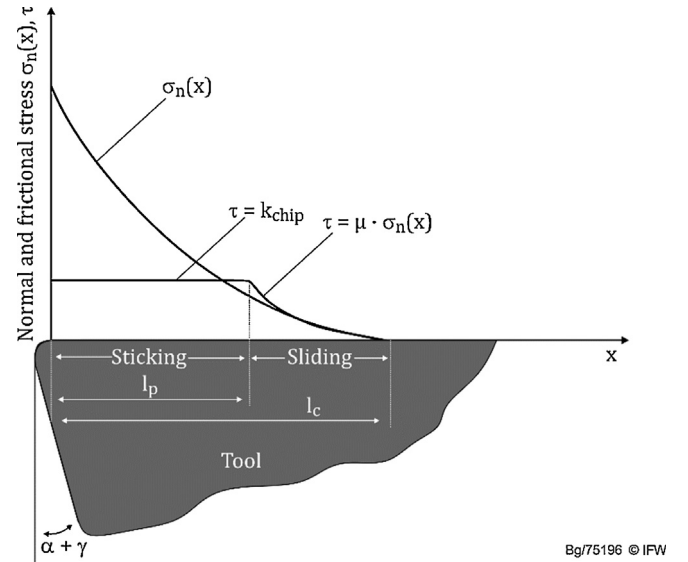


Fig. 6. Normal and frictional stress distribution over the rake face [35].

Validation of material model

As indicated, the material models by Umbrello et al. and Yan et al. represent the material hardness and thus are suitable for modelling hard machining. However, to identify a suitable material model in the first step the simulated process forces were compared with the experimental process forces for the hard milling process in this study. As previously shown, the friction has to be considered. In order to calibrate the simulation, the friction is investigated in a wide range. In addition, for a validation of the simulated tool stresses, which are essential for the design of cutting edge geometries, an approach is presented. Wherein the tool failure is compared to the calculated tool stresses in the FEM simulation. The measurement of the process forces was conducted in full immersion face milling operations to avoid an increase in the process forces on tool entry, which occurs at half immersion milling operations. In Fig. 7 the process forces are shown after coordinate transformation from the X-, Y- and Z-direction.

As illustrated in Fig. 7a, the maximal force results at 90° feed motion angle φ as a result of the maximal value of the undeformed chip thickness h . Furthermore, the main force component is represented by the force in axial direction F_p , because of the small value of the cutting edge angle κ , which shifts the force to the axial direction. In the first step the process forces for the applied friction models were compared at the maximum value for the effective undeformed chip thickness at tool entry, point 1 in Fig. 7a, and the reference machining parameters. The simulated force in X-direction was squared with the cutting force F_c and the simulated force in Y-direction with the thrust force F_D referring to κ_{eff} , which is the assumed orthogonal plane (Fig. 7c). The thrust force F_D was calculated according to Eqs. (22)–(25). The force transformation has to be done in order to transfer the milling process to the simulation (orthogonal turning process). In the FEM simulation, an orthogonal turning process is modelled. In comparison to the face milling process, the orthogonal turning process presents a reduced number of force components. In order to compare the simulated process forces with the measured process force, a parameter transformation was carried out. This has been done through the use of their respective orthogonal plane and referring the process forces to the cross-section of undeformed chips (Fig. 7b and c). Thereby the measured process forces were referred to the cutting

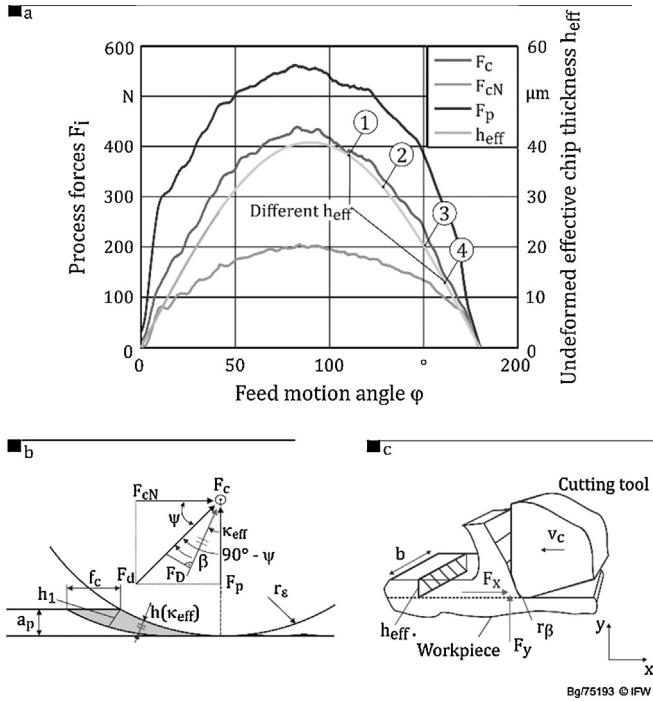


Fig. 7. (a) Measured process forces and effective undeformed chip thickness in hard milling AISI H13; (b) Transformation of process forces (c) Orthogonal plane of the milling process at h_{eff} .

edge b_{eff} (Eqs. (26) and (27)). The analogous process value was determined in the FEM simulation through the forces in X- and Y-direction with respect to the width of undeformed chip b . The default value of b is $b = 1$ mm.

$$F_d = \sqrt{F_{cN}^2 + F_p^2} \quad (22)$$

$$\Psi = \tan^{-1} \frac{F_p}{F_{cN}} \quad (23)$$

$$\beta = 90^\circ - \Psi - \kappa_{eff} \quad (24)$$

$$F_D = \cos \beta \cdot F_d \quad (25)$$

$$\frac{F_c}{b_{eff}} = \frac{F_x}{b} \quad (26)$$

$$\frac{F_D}{b_{eff}} = \frac{F_y}{b} \quad (27)$$

The comparison of the measured and simulated presents Fig. 7. As a result it can be seen, that higher friction leads to higher simulated process forces, but their relationship depends on the used friction law. According to the material models of Umbrello et al. and Yan et al., the simulated forces in X-direction (Cutting force) are similar to each other. In contrast to the simulated forces in X-direction (Cutting force) the forces in Y-direction exhibit differences. Compared with the measured process forces either the thrust force or the cutting force can be adjusted by the friction law. However, according to different friction laws one force component is still over or under depicted. Minor deviations to the process forces for different friction laws and material models are summarized in Fig. 8.

As displayed in Fig. 8 the cutting force can be simulated with minor deviations. The best result for simulating the process forces is with $m = 0.6$, which is independent from the material model. The maximum differs by about 5%, whereas the thrust force is

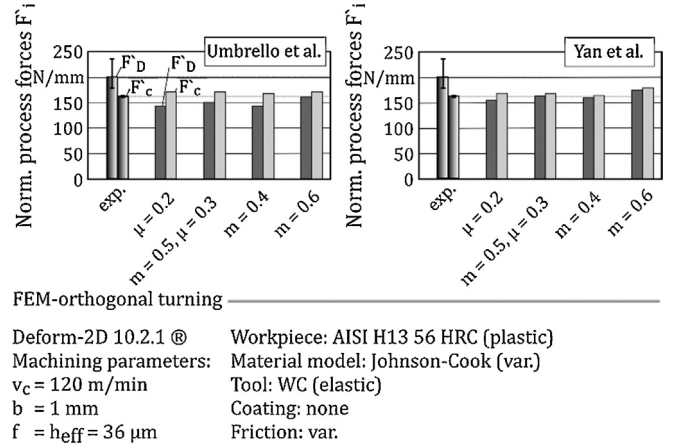


Fig. 8. Comparison between measured process forces and simulated process forces.

underestimated. According to Yen et al. these differences for the simulated thrust forces can be attributed for different reasons. Firstly, the extrapolations of the flow stress data to higher strain, strain rates and temperature out of the flow data range occur in errors. Secondly, the derivatives are a result of the friction law, which does not depict the processes at the tool tip [18].

In order to predict the measured cutting forces, based on these results, further simulations at feed motion angles 2–4, see Fig. 7a, with the friction laws in Fig. 8 were conducted. Because of the fact, that by the previous simulation both material models seem to be suitable. Feed motion angles 2–4 are equal to $h_{eff2} = 30$ μm, $h_{eff3} = 20$ μm, $h_{eff4} = 7$ μm, see Fig. 7a. For both material models the best result was achieved for the shear friction law with $m = 0.6$. In Fig. 9, however, the comparison of simulation and experiment for the developed material model by Umbrello et al. is summarized.

It can be seen that the simulated cutting forces show a good agreement with the measurements. Whereas, according to the thrust force derivatives are reduced with decreasing effective undeformed chip thickness. This may be due to the flow stress data, which represents the material in a compressive state rather than in a sheared state [36].

However, besides the process forces the stresses in the tool are important to develop different cutting edge geometries. In order to develop an undercut geometry it requires the knowledge of the maximal tool load at milling operations. For determining the highest tool load, the mechanical and thermo load were analyzed with the simulation at different feed motion angles. In contrast to simulate the process forces, regarding the thermo-mechanical load the maximal undeformed thickness h_1 was applied. It is assumed that the highest specific load occurs along the cutting edge at the location of the maximum undeformed chip thickness. As can be further seen in Fig. 10, that the maximal thermo-mechanical load occurs at the tool entry due to the maximum undeformed chip thickness.

With further increase of the rotation angle and simultaneous decrease of maximum chip thickness, both, mechanical and thermo load decrease. Here, the simulated temperature is more a relative value, which was not verified with tool temperature measurements. Nevertheless, this means that the critical load occurs at tool entry, respectively maximum undeformed chip thickness h_1 . Based on Fig. 10, the stresses for various undercut geometries were analyzed at the maximum chip thickness h_1 at tool entry. Afterwards, to identify a suitable material model, a regression model with a constant chip thickness h_1 was calculated on the basis of chip formation simulations with different undercut

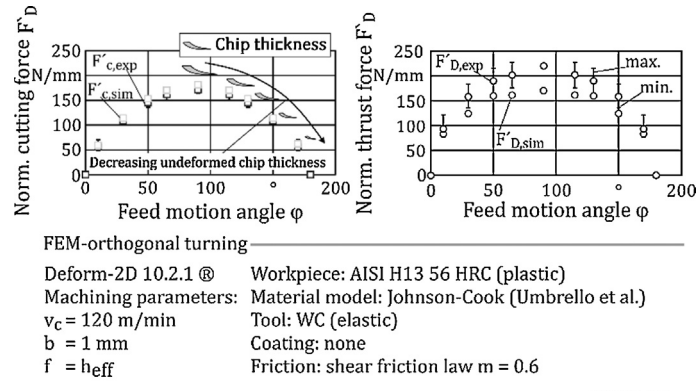


Fig. 9. Comparison between measured process forces and simulated process forces regarding the feed motion angle.

modifications for both material models. Both previous material models offered a sufficient accordance regarding the process forces. In these FEM simulations the undercut geometries were varied for the width of undercut S_b from 60 to 140 μm , for the depth of undercut S_t from 70 to 110 μm , for the radius in the undercut r from 40 to 100 μm and for the angle of the undercut α between 30 and 100° (compare Fig. 1). To evaluate the load on the tool, the principal stress hypothesis was used. The application of this failure criterion for brittle materials has been used in terms of analysing the failure of cutting tools in machining operations, among others by Denkena [12], Scherbarth [13] and Loladze [37]. The principal stress failure criterion in machining is typical used in order to explain tool failure due to an exceeding maximum principle stress of the ultimate tensile strength. Especially cemented carbide tools and other hard cutting tools exhibit reduced ultimate tensile strength in comparison to compressive strength. However, in terms of the undercut geometries only compressive stresses were found within the undercut. Due to this, in this study it is assumed, that tool failure occurs when the minimum principal stress σ_{\min} exceeds the compressive strength of the cemented carbide σ_{db} . The compressive strength of the carbide grade H10 can be assumed with a value of $\sigma_{\text{db}} = 6500 \text{ MPa}$ [26]. The calculated regression models for both material models with constant chip thickness are based on a linear, quadratic approach. The coefficient of determination for both models is $R^2 > 0.96$. In order to identify the material model, which represents the load on the tool, 14 different undercut geometries were manufactured by laser machining. Afterwards, these tools were applied in hard milling with the reference machining parameters, to analyze tool failure. The tools were analyzed after a cutting path of cutting length of $l_f = 100 \text{ mm}$. During this period of use it is to be

assumed that no reduction in the compressive strength results due to the dynamic load. By using the regression model with the material model by Umbrello et al., 13 out of 14 failures were predicted, which is a rate of 92.8%. In contrast, the regression model based on the material model by Yan et al. yielded an agreement with the experimental results of 42.8% (6 out of 14). This fact can be traced back to the higher simulated process forces. Principally, the higher cutting force causes increased minimal principal stresses in the undercut. Thus, it should be noted that the material model by Umbrello et al. predicts the thermo-mechanical load with a higher accuracy.

For modelling various loads and thus the use of the undercut geometries under different machining parameters, the regression model was expended for an undeformed chip thickness of $h_1 = 36 \mu\text{m}$ to $h_1 = 80 \mu\text{m}$ (Eq. (28)). The cutting speed was not varied.

$$\sigma_{\min} = a \cdot h + b \cdot \alpha + \frac{c}{h} + \frac{d}{\alpha} + \frac{e + f \cdot S_t + \alpha^2 - g \cdot S_t \cdot \alpha}{S_b + r} - i \cdot S_b \quad (28)$$

The parameters and their values for Eq. (28) are summarized in Table 5.

The calculated regression model was carried out with the software tool “Eureqia” developed at the Cornell University. Due to symbolic regression the software determines mathematical equations with respect to the input data. The mathematical equations are optimized in order to reduce the various error metrics. Fig. 11 demonstrates the correlation between the modelled and simulated minimal principal stresses for various geometries, different undeformed chip thicknesses h_1 and constant cutting speed of $v_c = 120 \text{ m/min}$. The different undeformed chip thicknesses h_1 can be adjusted for example due to the feed f .

With a coefficient of determination of $R^2 = 0.98$ a high correlation was achieved. The verification of the regression model was done analogue to the verification for the regression model for a constant chip thickness. With a match of 94.3%, the failure of the

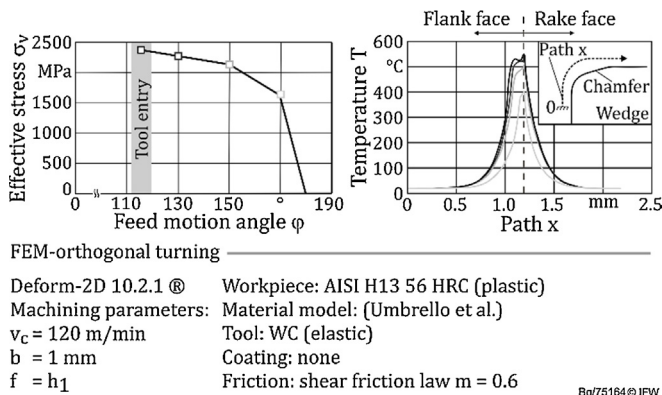


Fig. 10. Thermo-mechanical load over feed motion angle ϕ .

Table 5
Constants for the regression model.

Parameter	Value
a	43.38
b	16.51
c	$2.502 \cdot 10^4$
d	$-5.182 \cdot 10^4$
e	$7.518 \cdot 10^4$
f	$1.206 \cdot 10^4$
g	189.3
i	3.558

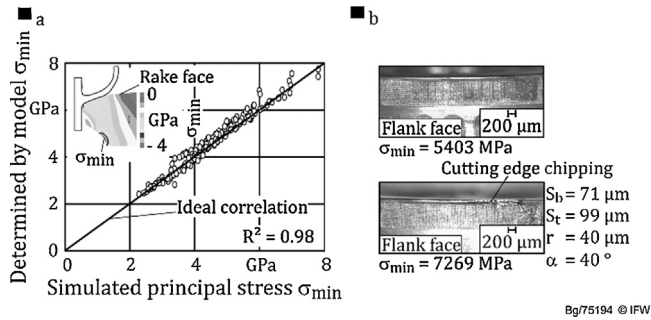


Fig. 11. (a) Developed model for calculating the minimal principal stress; (b) Results of cutting tests.

tools could be predicted with the developed model in use of 35 experimental cutting experiments, which are exemplary demonstrated in Fig. 11b. Fig. 11b presents two different undercut geometries. With a value of principal stress, less the compressive strength ($\sigma_{min} = 5403$ MPa), no chipping occurs. Whereas at stress values of $\sigma_{min} > 6500$ MPa, presented by Fig. 11b in the bottom, cutting edge chipping can be observed.

Experimental results for modified flank face geometries

Tool wear

The wear behaviour of the reference tool is shown in Fig. 12. Distinctive flank wear occurs in hard milling of AISI H13. A uniform abrasive flank wear and adhesion were observed, presented in Fig. 12b. A good repeatability of the tool wear behaviour was achieved. The discrepancy of both experiments could be determined of $VB_m = 10 \mu m$ with respect to the flank wear. To guarantee repeatability and uniform flank wear workpiece chamfer and roll on entry have been applied. Due to roll-in-entry the uncut chip thickness in the tool entry is reduced to zero. Hereby tensile stresses at tool exit can be avoided [38]. The chamfer on the workpiece steadied a smoother tool entry in the first milling path.

At first, to ensure that the removal of the coating due to flank face modification by laser ablation had no impact on the wear behaviour, tools with coating and tools without coating after preparation were compared. For comparability, a geometrically identical undercut geometry was applied. Afterwards, both tools

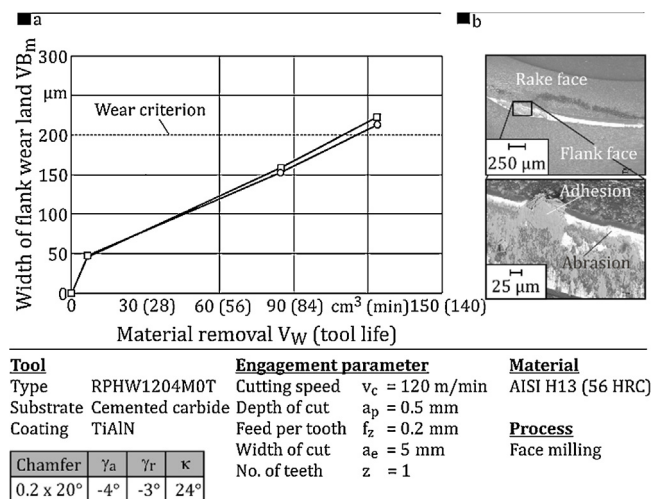


Fig. 12. (a) Wear behaviour of the reference tools; (b) SEM pictures at the end of tool life time for the reference tools.

were investigated under the reference machine parameter. As a result, in terms of tool life itself, the differences are negligible. Furthermore, the main wear mechanisms abrasion and adhesion were analyzed for both tools, with additional coating in the undercut and coated tools without coating in the undercut. It can be concluded, that an additional coating after flank face preparation does not influence the tool life in comparison to coated without a subsequent coating in the undercut. For tool life investigations three approaches using different undercuts, as shown in Fig. 13, were applied. As previous shown in Figs. 9 and 10, the thermo-mechanical load depends on the undeformed chip thickness. In order to influence the stability of the cutting edge and the tool wear progression different approaches were pursued.

In the first approach the undercut with a constant width of undercut S_b along the cutting edge was prepared (Tool 1). In the second approach the cutting tool was modified with varying width of undercut S_b along the cutting edge. Thereby, a larger width of undercut towards higher chip thickness was applied. Furthermore, in this approach the depth of the undercut was designed with a rounding (Tool 2) and a chamfer (Tool 3). For the last approach, the flank face was only modified at the surface-generating part of the cutting edge (Tool 4). The depth of undercut was designed as a combination of a rounding and a chamfer. The various approaches for the undercut of the flank face were investigated under the reference machining parameter with two repetitions. As a result, the highest increase of tool life could be achieved with Tool 4, see Fig. 13. Fig. 14 displays the effect of the undercut. Due to the usage of a higher depth of undercut S_t , the tool wear progression is slowed down over a certain cutting time. The increased depth of undercut S_t could be applied due to the decreased thermo-mechanical load in the surface generated part of the cutting edge. Despite an increase of S_t regarding the stability of the cutting edge is comparison to the reference tool the wear progress is decreased over a certain cutting time. Consequently, according to the reference tool a maximum increase of tool life up to 100% could be realized. In addition, the modified cutting tools show a similar uniform abrasive flank wear as the reference tools.

Two repetitions were conducted. For these three experiments, an average of an increase tool life up to 86% was achieved, with a maximum discrepancy of $T = 14\%$.

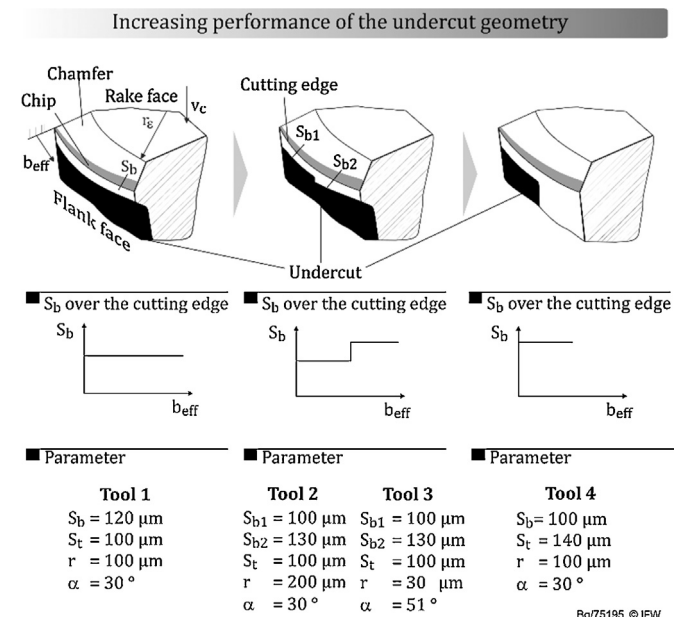


Fig. 13. Different approaches for undercut geometries.

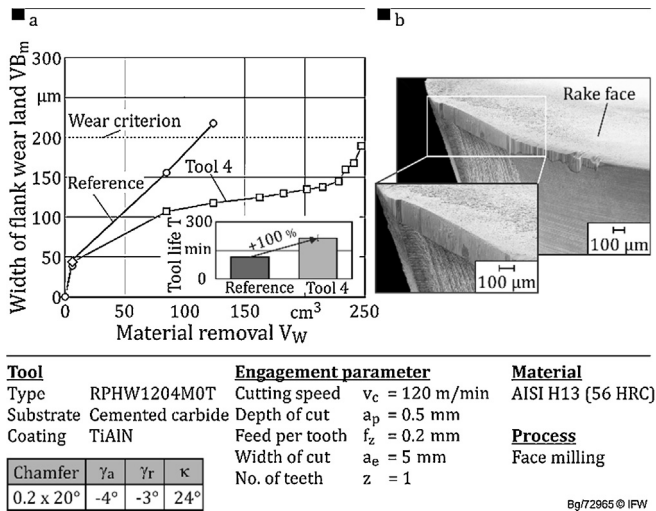


Fig. 14. Influence of the undercut on the tool lifetime; (b) SEM pictures at the end of tool life time (Tool 4).

The same undercut was further investigated under different cutting speeds. Increased cutting speed was chosen, because of the impact of the cutting speed on the tool life. With the developed undercut geometry increased tool life was achieved even at increased cutting speeds. However, the gain of tool life decreases with higher cutting speed (Fig. 15). Due to increased cutting speed the thermal load rises. This leads to reduced tool life time. Furthermore, with increasing cutting speed chipping on the cutting edge occurs due to the enhanced dynamical load on the cutting edge, see Fig. 15. The higher dynamical load is the result of the increased chip segmentation. With increased feed per tooth f_z no gain of tool life could be achieved. Due to higher mechanical and dynamical load tool failure occurs. With increased feed per tooth higher chip segmentation and increased mechanical load, due to the increased undeformed chip thickness, occur. As a consequence, the cutting edge fails.

Surface integrity

Due to the undercut of the flank face, improved residual stresses could be achieved in comparison to the reference tools. Fig. 16

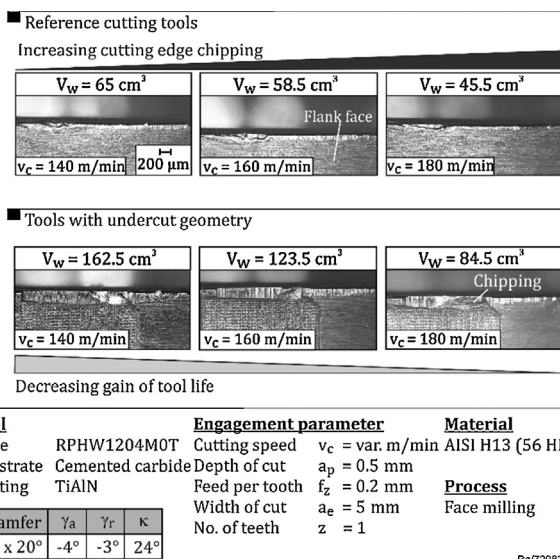


Fig. 15. Increasing gain of tool lifetime with increasing cutting speed.

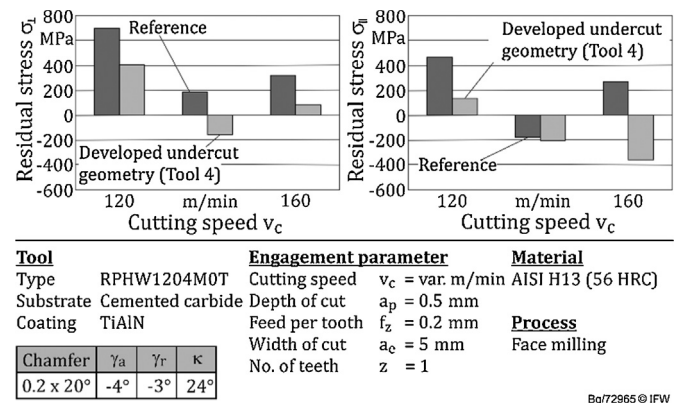


Fig. 16. Influence of the undercut on residual stresses.

Table 6

Process forces at the end of tool life time for the reference tools in comparison to the developed undercut geometry.

Tools	Passive force F_p	Feed normal force F_{FN}	Feed force F_f
Reference tool	1218 N	524 N	294 N
Developed undercut geometry	966 N (−26%)	472 N (−11%)	136 N (−116%)

represents the values of the superficial residual stresses measured via X-ray diffraction at the end of the reference tool life ($VB_m = 200 \mu\text{m}$). Fig. 15 presents a significant reduction of the surface tensile residual stresses in both directions for the undercut geometries compared to the reference tools. This can be attributed to the significantly decreased width of flank wear land of the tools with an undercut. Here, the width of flank wear land leads to a reduced thermal load on the workpiece, and thus lower tensile residual stresses [39,40].

This is further proven by the process forces, measured at the same cutting time. Due to the reduced wear, friction decreased between tool and workpiece. In consequence, lower process forces result for the tools with a flank face modification, summarized in Table 6.

In contrast to the expectations of shifting the residual stresses towards tensile stresses with increasing cutting speed, these could not be verified in this study. Rather, the residual stresses decrease with increasing cutting speed. This can be attributed on the to varied shear due to the increased cutting edge chipping with higher cutting speeds. Simultaneously the cutting edge chipping leads to different contact conditions with the workpiece and leads to more plastic deformation and thus even measured compressive residual stress. Nevertheless, it has to be mentioned that the experiments were only carried out once and further research is necessary.

Conclusion and outlook

In this study, the design and the influence of undercut geometries in hard milling were investigated. The design of the undercut has been developed by using FEM chip formation simulations. An approach was shown, which enables to simulate milling processes with varying undeformed chip thickness along the cutting edge. The numerical and experimental process forces show a good agreement. This FEM simulation has been further used to establish a regression model that gives the undercut geometry for milling AISI H13 for a given parameter set, which is valid for undercut chip thickness from $30 \mu\text{m}$ to $80 \mu\text{m}$. Due to

the regression model the tool fracture for tools with a flank face modification can also be predicted. Undercut geometries on the flank face pose a significant influence on the wear behaviour of cutting tools in hard milling operations. The wear behaviour depends on the design of the undercut and location at the cutting edge. By applying the undercut geometry, increased tool life, up to 100%, was achieved. Under reference machining parameter a correlation of the residual stresses and process forces to the wear could be demonstrated. Moreover, improved surface residual stresses occur due to the undercut geometries at the end of the tool life compared to the reference tools. Further investigations on undercut geometries for different materials with respect to the wear behaviour and as well on surface integrity will be conducted.

Acknowledgements

The IGF-project (IGF – 17225N) of the Research Association (VDW – Forschungsinstitut e.V.) was supported by the AiF within the programme for the promotion of industrial research (IGF) from the Federal Ministry of Economy and Energy due to a decision of the German Bundestag. The authors would like to thank Seco Tools Germany for providing the cutting tools.

References

- [1] Altan, T., Lilly, B.W., Kruth, J.P., König, W., Tönshoff, H.K., van Luttervelt, C.A., Khairy, A.B., 2000, Advanced techniques for die and mold manufacturing, CIRP Ann: Manuf Technol, 42/2: 707–716.
- [2] Tönshoff, H.K., Arendt, C., Ben Amor, R., 2000, Cutting of hardened steel, CIRP Ann: Manuf Technol, 49/2: 547–566.
- [3] Tönshoff, H.K., Denkena, B., 2013, Basics of Cutting and Abrasive Processes, Springer, Berlin.
- [4] Brandt, D., 1996, Randzonenbeeinflussung beim Hartdrehen, (Dr. -Ing. Dissertation) Leibniz Universität Hannover.
- [5] Jochmann, S., 2001, Untersuchungen zur Prozess- und Werkzeugauslegung beim Hochpräzisionshartdrehen, (Dr. -Ing. Dissertation) RWTH Aachen.
- [6] Klocke, F., Kratz, H., 2005, Advanced tool edge geometry for high precision hard turning, CIRP Ann: Manuf Technol, 54/1: 47–50.
- [7] Müller, C., 2008, Prozessgrößen und Randzoneneigenschaften beim Drehen gehärteter Stähle, (Dr. -Ing. Dissertation) Leibniz Universität Hannover.
- [8] Meyer, R., 2011, Neue Schneidengeometrien zur Verbesserung des Werkzeug-einsatzverhaltens beim Hartdrehen, (Dr. -Ing. Dissertation) Leibniz Universität Hannover.
- [9] Denkena, B., Boehnke, D., Meyer, R., 2008, Reduction of wear induced surface zone effects during hard turning by means of new tool geometries, Prod Eng Res Dev, 2/2: 123–132.
- [10] Kobayashi, S., Oh, S.-I., Altan, T., 1989, Metal Forming and the Finite-element Method, vol. xvii. Oxford University Press, New York. p. 377.
- [11] Arrazola, P.J., Özel, T., Umbrello, D., Davies, M., Jawahir, I.S., 2013, Recent advances in modelling of metal machining processes, CIRP Ann: Manuf Technol, 62/2: 695–718.
- [12] Denkena, B., 1992, Verschleißverhalten von Schneidkeramik bei instationärer Belastung, (Dr. -Ing. Dissertation) Leibniz Universität Hannover.
- [13] Scherbarth, S., 1999, Der Einfluß der Schneidkeilgeometrie auf das Zerspanverhalten beim Fräsen von Stahlwerkstoffen mit beschichtetem Hartmetall, (Dr. -Ing. Dissertation) TU Hamburg-Harburg.
- [14] Zhou, J.M., Andersson, M., Ståhl, J.-E., 1997, Cutting tool fracture prediction and strength evaluation by stress identification. Part I: Stress model, Int J Mach Tools Manuf, 37/12: 1691–1714.
- [15] Chen, L., El-Wardany, T.I., Nasr, M., Elbestawi, M.A., 2006, Effects of edge preparation and feed when hard turning a hot work die steel with polycrystalline cubic boron nitride tools, Ann CIRP, 55/1.
- [16] Özel, T., 2003, Modeling of hard part machining: effect of insert edge preparation in CBN cutting tools, J Mater Process Technol, 141/2: 284–293.
- [17] Rech, J., Yen, Y.-C., Schaff, M.J., Hamdi, H., Altan, T., Bouzakis, K.D., 2005, Influence of cutting edge radius on the wear resistance of PM-HSS milling inserts, 15th International Conference on Wear of Materials, vol. 259 (7–12), pp.1168–1176.
- [18] Yen, Y.-C., Jain, A., Altan, T., 2004, A finite element analysis of orthogonal machining using different tool edge geometries, Containing Research Papers on Sheet Forming Machining and Tube Hydroforming, 146 (1). p. 72–81.
- [19] Shivpuri, R., 2005, Dies and die materials for hot forging, ASM Handbook, ASM International, USA. pp. 47–61.
- [20] Köhler, J., 2010, Berechnung der Zerspankräfte bei variierenden Spannungsquerschnittsformen, (Dr. -Ing. Dissertation) Leibniz Universität Hannover.
- [21] Kienzle, O., 1954, Einfluss der Wärmebehandlung von Stählen auf die Hauptschnittkraft beim Drehen Stahl und Eisen, vol. 74. p. 530–551.
- [22] Victor, H., Kienzle, O., 1952, Die Bestimmung von Kräften und Leistungen an spanenden Werkzeugmaschinen, vol. 94. VDI-Z. p. 299–305.
- [23] Westhoff, B., 2001, Modellierungsgrundlagen zur FE-Analyse von HSC-Prozessen, (Dr. -Ing. Dissertation) Universität der Bundeswehr Hamburg.
- [24] Filice, L., Micari, F., Rizzuti, S., Umbrello, D., 2007, A critical analysis on the friction modelling in orthogonal machining, Int J Mach Tools Manuf, 47/3–4: 709–714.
- [25] Shatla, M., Kerk, C., Altan, T., 2001, Process modeling in machining. Part I: Determination of flow stress data, Int J Mach Tools Manuf, 41/10: 1511–1534.
- [26] Brookes, K.J.A., 1996, World Directory and Handbook of Hardmetals and Hard Materials, 6th ed. International Carbide Data, East Barnet, Hertfordshire.
- [27] Johnson, G.R.W.H.C., 1983, A constitutive model and data for metals subjected to large strains, high strain rates and high temperatures, in: Proceedings of the 7th International Symposium on Ballistics, International Ballistics Committee, The Hague, Netherlands, pp. pp.541–547.
- [28] Ng, E.-G., Aspinwall, D.K., Brazil, D., Monaghan, J., 1999, Modelling of temperature and forces when orthogonally machining hardened steel, Int J Mach Tools Manuf, 39/6: 885–903.
- [29] Oxley, P.L.B., 1989, Mechanics of Machining, An Analytical Approach to Assessing Machinability, Ellis Horwood, Chichester.
- [30] Umbrello, D., Rizzuti, S., Outeiro, J.C., Shivpuri, R., M'Saoubi, R., 2008, Hardness-based flow stress for numerical simulation of hard machining AISI H13 tool steel, J Mater Process Technol, 199/1–3: 64–73.
- [31] Yan, H., Hua, J., Shivpuri, R., 2007, Flow stress of AISI H13 die steel in hard machining, MaterDes, 28/1: 272–277.
- [32] Childs, T.H.C., 2006, Friction modelling in metal cutting. Tribology in manufacturing processes, 2nd International Conference on Tribology in Manufacturing Processes, vol. 260 (3), pp.310–318.
- [33] Shaw, M.C., 1984, Metal Cutting Principles, Clarendon Press, Oxford.
- [34] Arrazola, P.J., Özel, T., 2010, Investigations on the effects of friction modeling in finite element simulation of machining, Int J Mech Sci, 52/1: 31–42.
- [35] Zorev, N.N., 1963, Interrelationship Between Shear Processes Occurring Along Tool Face and on Shear Plane in Metal Cutting, ASME International Research in Production Engineering, ASME, 42–49.
- [36] Al-Zkeri, I., Rech, J., Altan, T., Hamdi, H., Valiorgue, F., 2009, Optimization of the cutting edge geometry of coated carbide tools in dry turning of steels using a finite element analysis, MachSci Technol, 13/1: 36–51.
- [37] Loladze, T.N., 1975, Nature of brittle failure of cutting tool, Ann CIRP, 24/1: 13–26.
- [38] Denkena, B., Köhler, J., Bergmann, B., 2013, Hartfräsen – prozesssicher und produktiv, vol. 9. VDI-Z. p. 60–63.
- [39] Brinksmeier, E., Cammett, J.T., König, W., Leskovaar, P., Peters, J., Tönshoff, H.K., 1982, Residual stresses – measurement and causes in machining processes, AnnCIRP, 31/2: 491–510.
- [40] König, W., Klinger, M., Link, R., 1990, Machining hard materials with geometrically defined cutting edges-field of applications and limitations, AnnCIRP, 39/1: 61–64.